metals

MDPI

Article

A Method for Simultaneous Optimization of Blank Shape and Forming Tool Geometry in Sheet Metal Forming Simulations

Bojan Starman [1], Gašper Cafuta [2] and Nikolaj Mole [1,*]

[1] Faculty of Mechanical Engineering, University of Ljubljana, Aškerčeva 6, 1000 Ljubljana, Slovenia; bojan.starman@fs.uni-lj.si
[2] Cafuta d.o.o., Kalce 5j, 1370 Logatec, Slovenia; gasper.cafuta@cafuta.eu
* Correspondence: nikolaj.mole@fs.uni-lj.si; Tel.: +386-1-4771-425

Abstract: This paper presents a numerical method for simultaneous optimization of blank shape and forming tool geometry in three-dimensional sheet metal forming operations. The proposed iterative procedure enables the manufacturing of sheet metal products with geometry fitting within specific tolerances (surface and edge deviations less than 0.5 or 1.0 mm, respectively) that prescribe the maximum allowable deviation between the simulated and desired geometry. Moreover, the edge geometry of the product is affected by the shape of the blank and by an additional trimming phase after the forming process. The influences of sheet metal thinning, edge geometry, and springback after forming and trimming are considered throughout the blank and tool optimization process. It is demonstrated that the procedure effectively optimizes the tool and blank shape within seven iterations without unexpected convergence oscillations. Finally, the procedure thus developed is experimentally validated on an automobile product with elaborated design and geometry which prone to large springback amounts owning to complex-phase advanced high strength steel material selection.

Keywords: sheet metal forming; blank shape; tool design; optimization; experimental validation

Citation: Starman, B.; Cafuta, G.; Mole, N. A Method for Simultaneous Optimization of Blank Shape and Forming Tool Geometry in Sheet Metal Forming Simulations. *Metals* **2021**, *11*, 544. https://doi.org/10.3390/met11040544

Academic Editor: Ricardo J. Alves de Sousa

Received: 5 March 2021
Accepted: 24 March 2021
Published: 26 March 2021

1. Introduction

Mass production of manufactured sheet metal goods is nowadays subject to high standards of quality that impose strict requirements regarding the geometric tolerances and visual quality of the final product. To achieve these objectives, the forming process must be designed carefully and mastered effectively, also taking into account time consumption and financial expenses [1]. To minimize the use of trial and error approaches and consequently the costs of tool production, computer-aided design procedures can be utilized; in these procedures, *Finite Element Method* (FEM) simulations of a forming process, for example [2], play the central role [3]. While FEM simulations serve primarily as a tool for investigating the feasibility of a forming process in the sense of avoiding sheet metal defects [4], they can also be employed as a part of the forming tool, blank shape [5], or blank thickness optimization procedures with the aim of achieving proper geometrical acceptability of the product. This enables the minimization of tool production costs through reducing the number of tool modifications or even eliminating some forming stages, such as the trimming phase [6]. With FEM simulations, the process can also be optimized for the use of thinner sheets [7], all to decrease financial expanses.

A proper blank shape also requires less material for production and may reduce the occurrence of manufacturing defects during the forming process, such as tearing and wrinkling. However, a certain portion of the product shape area usually needs to lie under the holder in order to achieve a sufficiently secure hold on the blank, resulting in an unavoidable sheet trimming phase after the forming process. Where the trimming phase can be eliminated, however, the accuracy of the product edge geometry depends highly on the proper design of the blank geometry. Sheet metal thinning during forming and springback, which is always present due to the elastoplastic response of the sheet metal

during the forming process, can be controlled by modifying the forming tool design. The amount of springback plays a special role when simulating the response of high strength steels, owing to the high yield stress and the consequently larger elastic strains that need to be compensated after tool removal [8]. Due to the high formability of these steels, there are also greater differences in wall thickness [9]. Springback can also be compensated by increasing the blank-holder force, but due to proportional force magnitude and product thinning this is not a general remedy. An intriguing process of springback compensation using *Magnetic Pulse Forming* has recently been described in a work by Cui et al. [10].

In this paper, we present a procedure for the simultaneous optimization of forming tool and blank shape geometry that involves adjusting the potential geometrical deviations of the product shape from its desired shape as defined in the form of the general 3D geometry by the product designer. In the procedure, the optimal forming tool design and blank geometry are determined iteratively, taking the desired product geometry as the initial tool geometry into account. The initial blank geometry is determined approximately from experience. Moreover, the methodology is also extended to products where the sheet trimming phase is unavoidable. In these cases, the product edge is partly defined by the forming and trimming phase. However, the trimming line is considered in the optimization procedure.

2. State of the Art

The proposed methodology originates from the *Displacement Adjustment* (DA) method, originally proposed by Gan and Wagoner [11]. The concept of the method involves adjusting the nodes defining the tool surface in the direction opposite to the springback error. In the method, the product is defined by using 2D shell finite elements to model the product's mid-surface. The adjustment is performed iteratively, where the tool geometry compensation is applied in the direction parallel to the punch travel. While the method is simple and relatively straightforward, several improvements have been proposed—recently, for example, by Ma et al. [12]. One of the first improvements was proposed by Lingbeek et al. [13] to resolve the issue of different topological structures of tool and blank geometry by using smooth surfaces. In the paper, they also proposed an alternative method where the adjustment is based on CAD geometry but they concluded that both methods need further improvements to allow industrial application. In order to increase the robustness of the method, Meinders et al. [14] introduced adjustment correction determined based on the residual stress state in the product. Similarly to [13], Lan et al. [15] proposed a generalisation of the DA method by using NURBS to construct a smooth tool surface and demonstrated that their method is an effective tool for producing accurate complex-shaped sheet metal products. A similar approach was also employed by Lu et al. [16], who optimized the forging tool by also taking into account its deformability.

The predicted product geometry and corresponding tool adjustment due to springback are highly dependent on the material model employed [17]. Taking into account sheet metal anisotropy, Yang and Ruan [18] improved the DA method by considering compensation direction, which plays a key role in springback compensation. Generally, a tool point topology after springback compensation along a certain direction may differ from the desired tool geometry [19], resulting in a position error, which is neglected in most cases [20]. To improve springback compensation, Cimolin et al. [21] proposed an optimization method where the product geometry after springback is described as a sum of initial tool geometry and associated shape functions. The role of the shape functions is to yield the most appropriate change of the initial tool geometry when the optimization algorithm is applied.

The method proposed by Karafillis and Boyce [22] is the most intriguing among the DA alternatives. In the first step of the method, a blank is deformed into the desired product shape and the nodal forces are recorded. In the next, the so-called *"springforward"* step, the shape thus derived is elastically loaded so as to obtain the tool geometry. The accuracy of the tool shape is checked by forming and springback simulation. If the resulting product shape deviates from the optimal shape, another iteration takes place, where the

blank is deformed to the tool geometry obtained in the previous iteration instead of being formed to the desired geometry. As the initially proposed method is valid only for axisymmetric products where no material draw-in was allowed, the authors also proposed a generalization [23]. Among other improvements, we should mention also the *Modified Springforward Method* by Cheng et al. [24]. However, the methods are limited to products with constant cross-sections (2D problems).

One of the major issues in springback is the compensation of 3D geometry. Owing to the many difficulties that arise from increasing nonlinearity, adjustment direction, and surface description, the classical approach is to optimize the process parameters, such as blank-holding force, the location and shape of the holder, selective lubrication, tool parts, and kinematics. For some examples, please see [25,26], and recently [27–29]. Since these problems are often solved through optimization algorithms, a large number of computer simulations of the forming process are needed. The number of the simulations can be reduced by using the *Response Surface Method*, which predicts the value of a cost function by using, e.g., a line search algorithm. The reader can obtain more information on this method in the papers of Wei et al. [30] and Schenk and Hillmann [31].

An intriguing method called the *Physical Scaling Approach* has recently been proposed by Birkert et al. [32]. The procedure uses the locally existent membrane stresses that result in the contraction of an elastic part to scale the drawing tool. By doing so, the root cause of the problem itself is directly used to solve the problem.

As reviewed, improvements for a functional approximation of discrete surface description and adjustment direction correction have been proposed in the literature. With regards to the latter, an accurate determination of surface normals from a discrete surface point topology is an essential step [33,34]. Consequently, when dealing with 3D springback compensation, an appropriate correspondence between the product and the tool topologies must be established. In our previous works [35,36], this was achieved through improved normal description—surface description is improved to achieve C^1 continuity when a rectangular surface mesh is used. Moreover, besides springback compensation, the product's wall thickness is also optimized by taking into account that the inner and the outer side of the product interact with the adjusted tool (see also Bici et al. [37]).

In addition to springback compensation, it is also beneficial, where applicable, to adjust the blank edge geometry to ensure that the formed product edge fits the desired shape. We have found various studies addressing this issue; prevalent methods include geometric mapping, direct [38], inverse [39], ideal forming, constrained optimization, neural network, deformation path, and volume addition/subtraction.

Azaouzi et al. [40], for example, used an inverse FEM simulation approach to estimate the initial blank shape in the first stage; this was followed by updating the blank shape through iterations combining standard optimization algorithms and direct FEM simulations. Similarly, Naceur et al. [41] used an evolutionary algorithm—chosen for its simplicity and efficiency—for the topological optimization of the structures. A two-stage procedure was also used by Park et al. [42]. In the first stage, a blank edge geometry is determined by employing the ideal forming theory [43]. An optimal blank geometry is subsequently obtained through the developed path iteration method in which the shape is adjusted based on the addition/subtraction of an amount of volume along with the deformation path. A combined approach was used also by Yeh et al. [44], who used the *Inverse True Strain Method* to obtain the initial blank shape. They used the *Adaptive-Network-based Fuzzy Interface System* to determine the anisotropic material optimum blank shape in the flange stretch process. A similar approach was taken also by Lin and Kwan [45], who used abductive networks to predict the optimum blank contour of an elliptic cylindrical cup without an earing profile after deep drawing. A generally known drawback of both these methods is that the optimization process could require a large number of FEM calculations, which may be time-consuming.

Son and Shim [46] proposed a direct method where the optimal blank shape is designed using the initial nodal velocity, which is used to calculate a scaling factor applied

to the correction of blank edge geometry. They found the method very effective in the design of an arbitrary drawing process. Particularly appropriate is the method by Hammami et al. [47]. They introduce a geometric mapping method where the blank is optimized using the *push/pull technique*. For the shape error selected, the method estimates the optimal blank shape within five iterations. Slightly better still is the method proposed by Fazli and Arezoo [48], where the correction of the blank shape is also based on taking into account the displacement path of the product edge nodes.

The optimal blank shape can also be obtained by parameterizing the blank geometry and applying classical optimization algorithms to find the optimal set of parameters [49]. Padmanabhana et al. [50], for example, used parametric *NURBS* curves and optimized the blank shape geometry by using the displacement of control points. The convergence of the method can be further improved by including the sensitivity of the optimization parameters [51].

In Mole et al. [52], we developed a geometric mapping method similar to the push/pull technique. One thing common to all the previously mentioned methods is that the blank must be re-meshed after its shape correction. In our method, by contrast, the mesh element topology is kept unchanged throughout the iterative procedure.

The challenge becomes evident when simultaneous springback compensation, thinning compensation, and blank edge geometry correction are required to achieve the product's desired shape. This means that the methods for springback compensation and blank edge geometry correction need to be integrated somehow. To the best of the authors' knowledge, no study has yet integrated springback, thinning, and blank edge geometry correction in a unified algorithm; this represents the main novelty of this paper.

3. Preliminaries

A sheet metal forming process generally involves the interaction of multiple tool parts with the sheet metal under kinematically driven conditions to form the final product. In computer simulations of such a process, the tool is usually modelled as a rigid surface, described analytically or discretely. If the sheet metal is relatively thin, a shell finite element model can be employed, but it should be emphasized that the response is not only driven by the process parameters but also by the material model.

Generally, the shape of the final product is achieved in multiple forming stages, which are followed by the springback after tool removal. Discrepancies between the product geometry achieved through forming and the desired product geometry should be minimized with the developed optimization methodology.

The methodology involves several numerical procedures, which are employed frequently throughout the optimization, and are described in this section.

3.1. Surface and Edge Topology

A typical simulation involves multiple tool parts and the sheet metal in surface contact interaction. In this paper, we define surfaces with discrete surface point topology $\mathcal{G}$, where the basic constituent of the surface is a quadrilateral subsurface joined by four adjacent points, resulting in a quadrilateral mesh representation of the surface.

We designate the tool surface point topology as $\mathcal{G}_{\text{tool}}$, blank mid-surface point topology as $\mathcal{G}_{\text{bl}}$, and the desired (or reference) product mid-surface topology as $\mathcal{G}_{\text{ref}}$. Since the FEM simulation typically consists of a forming and a relaxation step, we designate actual simulated mid-surface point topology as $\mathcal{G}_{\text{sim,m}}$ and mid-surface before springback occurs as $\mathcal{G}'_{\text{sim,m}}$. Since any forming process results in thickness reduction, it is essential to model tool–sheet interaction by using the top or bottom shell surface, dependent on a contact direction. We designate this surface point topology as control surface topology $\mathcal{G}_{\text{sim,cs}}$ and topology before springback as $\mathcal{G}'_{\text{sim,cs}}$. Moreover, when taking particular steps, the methodology requires the construction of an auxiliary surface, which we denote as $\mathcal{G}_{\text{aux}}$ surface point topology.

Blank shape optimization is based on edge topology manipulation; thus, we designate blank edge point topology as $\Gamma_{\text{bl}} \subset \mathcal{G}_{\text{bl,m}}$. The desired product edge topology is denoted as $\Gamma_{\text{ref}} \subset \mathcal{G}_{\text{ref,m}}$ and the edge topology of the simulated product as $\Gamma_{\text{sim}} \subset \mathcal{G}_{\text{sim,m}}$.

Throughout the paper, we use indices i or j that designate the i-th or j-th element $\square_i$ (or $\square_j$) of a set. Since the optimization is an iterative process, we use upper index $\square^{(k)}$ to designate the quantities or objects in the k-th iteration.

3.2. Surface and Edge Normals

3.2.1. Surface Normals

The basic procedure that is called several times in the tool and blank shape optimization process is surface and edge normals determination. Since the projected surface is defined by a point topology $\mathcal{G}$, the surface normal is determined at each i-th point P_i of topology $\mathcal{G}$, $P_i \in \mathcal{G}$. To improve the robustness and convergence of the general optimization algorithm, a two-stage procedure for improved normal description is proposed. In the first stage, to deal with the problem of duality [34], we define a normal vector $\boldsymbol{n}'_i$ at point P_i of the projected topology $\mathcal{G}$ as the average of normals $\boldsymbol{n}_{i,j}$ of N_i adjacent quadrilateral subsurfaces (or elements) $\mathcal{S}_j$ [53]. The normal $\boldsymbol{n}_{i,j}$ of the j-th adjacent element $\mathcal{S}_j$ can be determined by the cross product of the element's edge vectors $\boldsymbol{u}_{i,j}$ and $\boldsymbol{v}_{i,j}$ stemming from point P_i (c.f. Figure 1a). The normal $\boldsymbol{n}'_i$ determination can be formalized by the equation:

$$\boldsymbol{n}'_i = \frac{\sum_{j=1}^{N_i} \boldsymbol{n}_{i,j}}{\| \sum_{j=1}^{N_i} \boldsymbol{n}_{i,j} \|}, \quad \boldsymbol{n}_{i,j} = \boldsymbol{u}_{i,j} \times \boldsymbol{v}_{i,j}, \quad j \in \{1, 2, \ldots, N_i\}. \tag{1}$$

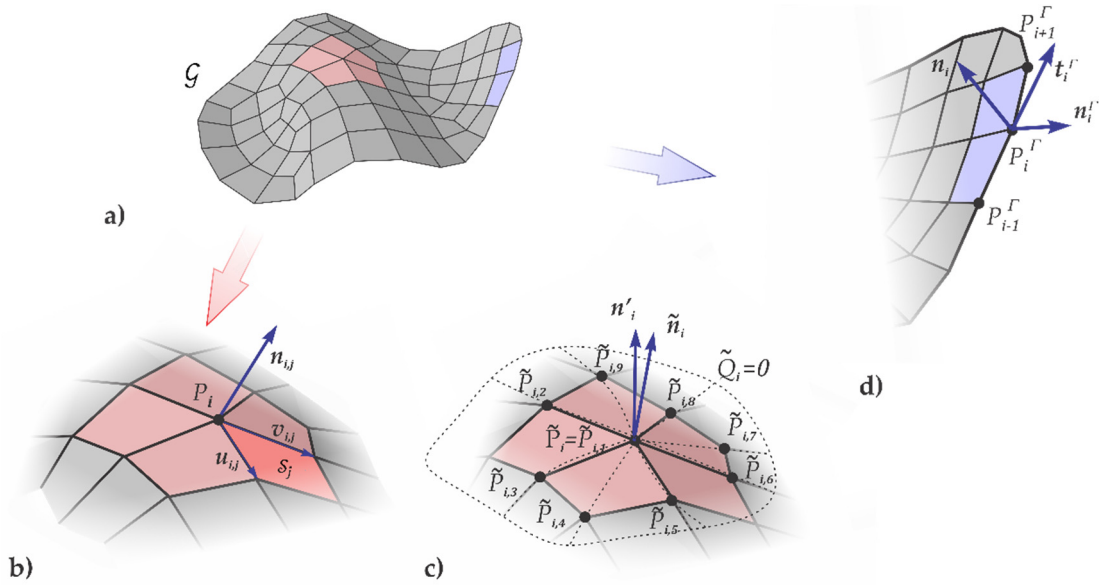

Figure 1. Determination of surface and edge normal vectors: (**a**) surface defined by its point topology, (**b**) the normal $\boldsymbol{n}_{i,j}$ of the j-th element $\mathcal{S}_j$ adjacent to P_i, (**c**) normal vector $\boldsymbol{n}'_i$ at point P_i as the mean of normals $\boldsymbol{n}_{i,j}$ of N_i adjacent elements, and normal vector $\tilde{\boldsymbol{n}}_i$ determined by polynomial surface approximation $\tilde{Q}_i(\tilde{x}, \tilde{y}, \tilde{z}) = 0$ through $\tilde{P}_{i,j}$ points, (**d**) edge normal $\boldsymbol{n}^{\Gamma}_i$ defined by the cross product of the tangential vector $\boldsymbol{t}^{\Gamma}_i$ and surface normal vector $\boldsymbol{n}_i$.

The main drawback of the description is that in the case of a surface with high curvature, or when the point topology is coarse, this approach would provide unsatisfactory results. To improve the description, a second stage is introduced. In this stage, the normal vector $\boldsymbol{n}_i$ is defined by the analytical surface $\mathcal{Q}_i$ [33] interpolated across the set of nine points of adjacent elements $\mathcal{S}_j, j \in \{1, 2, 3, 4\}$ (c.f. Figure 1b). In the case that more or less than four elements are connected at point P_i, nine closest points $P_{i,j}$ (including P_i) are chosen for surface formulation. The analytical surface formulation $Q_i(x, y, z) = 0$ is based on polynomial approximation, where the coefficients are generally determined by

interpolation through points $P_{i,j}$. However, it is generally known that the robustness of the interpolation procedure can be improved by the formulation of $\mathcal{Q}_i$ in the local coordinate system, say $(\widetilde{x}, \widetilde{y}, \widetilde{z})$ with the origin at P_i. The local basis vectors can be defined as

$$\boldsymbol{e}_{\widetilde{x}} = \boldsymbol{k} \times \boldsymbol{n}'_i, \quad \boldsymbol{e}_{\widetilde{y}} = \boldsymbol{n}'_i \times \boldsymbol{e}_{\widetilde{x}}, \quad \boldsymbol{e}_{\widetilde{z}} = \boldsymbol{n}'_i, \tag{2}$$

where the basis vector $\boldsymbol{k} = (0, 0, 1)$ defines the direction of the global z-axis. The rotation of the global coordinate system to the local coordinate system is defined by angle-and-axis parameterization of the three-dimensional rotation matrix:

$$\mathbb{R}(\boldsymbol{r}, \theta) = \begin{pmatrix} \cos\theta + r_1^2(1-\cos\theta) & r_1 r_2(1-\cos\theta) - r_3\sin\theta & r_1 r_3(1-\cos\theta) + r_2\sin\theta \\ r_1 r_2(1-\cos\theta) + r_3\sin\theta & \cos\theta + r_2^2(1-\cos\theta) & r_2 r_3(1-\cos\theta) - r_1\sin\theta \\ r_1 r_3(1-\cos\theta) - r_2\sin\theta & r_2 r_3(1-\cos\theta) + r_1\sin\theta & \cos\theta + r_3^2(1-\cos\theta) \end{pmatrix}, \tag{3}$$

where $\boldsymbol{r} = (r_1, r_2, r_3) = \boldsymbol{e}_{\widetilde{x}}$ and $\theta = \arccos\left(\boldsymbol{k} \cdot \boldsymbol{n}'_i\right)$. Next, the coordinates of the points $P_{i,j}$ are mapped to the local basis according to

$$\widetilde{\boldsymbol{P}}_{i,j} = \mathbb{R}(\boldsymbol{r}, \theta) \cdot \left(\boldsymbol{P}_{i,j} - \boldsymbol{P}_i\right), \tag{4}$$

where $P_{i,j}$ presents the position vector of the point $P_{i,j}$ with respect to the global coordinate basis. With the $\widetilde{P}_{i,j}$ defining the coordinates of the point $\widetilde{P}_{i,j}$ in the local coordinate basis, the analytical surface $\widetilde{Q}_i(\widetilde{x}, \widetilde{y}, \widetilde{z}) = 0$ can be interpolated through points $\widetilde{P}_{i,j}$ by assuming that the surface takes the following functional form:

$$\widetilde{Q}_i(\widetilde{x}, \widetilde{y}, \widetilde{z}) = \widetilde{z} - \left(a_1 + a_2\widetilde{x} + a_3\widetilde{y} + a_4\widetilde{x}\widetilde{y} + a_5\widetilde{x}^2 + a_6\widetilde{y}^2 + a_7\widetilde{x}^2\widetilde{y} + a_8\widetilde{x}\widetilde{y}^2 + a_9\widetilde{x}^2\widetilde{y}^2\right) = 0. \tag{5}$$

By requiring that the surface formulation must meet the requirements at nine interpolation points $\widetilde{P}_{i,j}$, the coefficients a_j, $j \in \{1, 2, \ldots, 9\}$ can be determined by solving a system of linear equations. Finally, the normal vector in the local coordinate basis $\widetilde{\boldsymbol{n}}_i$ can be determined by taking the gradient operator at the origin $\widetilde{\boldsymbol{n}}_i = \nabla\widetilde{Q}_i\left(\widetilde{P}_i\right) / \|\nabla\widetilde{Q}_i\left(\widetilde{P}_i\right)\|$. The normal vector in the global coordinate basis $\boldsymbol{n}_i$ at the point P_i can be retrieved by the inverse mapping:

$$\boldsymbol{n}_i = \mathbb{R}^{\mathbf{T}}(\boldsymbol{r}, \theta) \cdot \widetilde{\boldsymbol{n}}_i. \tag{6}$$

As we will present later, the above procedure is essential for the calculation of simulated surface point topology $\mathcal{G}_{\text{sim}}$ deviation from the desired surface $\mathcal{G}_{\text{ref}}$ and for the procedures mapping a specific surface to a target surface.

3.2.2. Edge Normals

To compensate for the deviations of the simulated product edge topology Γ_{sim} from the desired product edge topology Γ_{ref}, it is essential to identify, for an arbitrary point P_i^Γ on the edge, edge normals $\boldsymbol{n}_i^\Gamma$ perpendicular to edge tangential vector $\boldsymbol{t}_i^\Gamma$ and surface normal $\boldsymbol{n}_i$. The tangential vector at an arbitrary edge point P_i^Γ can be determined by constructing position vectors of two adjacent points, say P_{i-1}^Γ and P_{i+1}^Γ (c.f. Figure 1c).

The $\boldsymbol{t}_i^\Gamma$ can be approximated using simple vector algebra as the normalized difference of position vectors P_{i+1}^Γ and P_{i-1}^Γ. Finally, the edge normal $\boldsymbol{n}_i^\Gamma$ can be calculated as the cross product of the tangential vector $\boldsymbol{t}_i^\Gamma$ and surface normal $\boldsymbol{n}_i$:

$$\boldsymbol{n}_i^\Gamma = \boldsymbol{t}_i^\Gamma \times \boldsymbol{n}_i, \quad \boldsymbol{t}_i^\Gamma = \frac{\boldsymbol{P}_{i+1}^\Gamma - \boldsymbol{P}_{i-1}^\Gamma}{\|\boldsymbol{P}_{i+1}^\Gamma - \boldsymbol{P}_{i-1}^\Gamma\|}. \tag{7}$$

In the optimization methodology, the procedure will be applied on edge geometries Γ_{sim} and Γ_{ref} to determine the final blank shape geometry.

3.3. Surface Topology Normal Projection Mapping

In the optimization methodology, it is essential to address the deviation between two surface point topologies or to map one surface point topology to the desired surface. Let

us call the surface topology that is mapped to a specific surface the *projected surface topology* $\mathcal{G}_{\text{proj}}$ and the desired surface, to which the surface is mapped, the *target surface topology* $\mathcal{G}_{\text{tar}}$. For example, when calculating the deviation between the product simulated surface topology $\mathcal{G}_{\text{sim,m}}$ and the product desired topology $\mathcal{G}_{\text{ref}}$, the former is the projected topology and the latter is the target topology. It is also worth noting that generally, these surfaces can have different topologies.

When mapping an arbitrary point P_i^{proj} on $\mathcal{G}_{\text{proj}}$ to $\mathcal{G}_{\text{tar}}$, (c.f. Figure 2), it is essential that the surface normal vector $\boldsymbol{n}_i^{\text{proj}}$ associated with the point is calculated by the procedure described in Section 3.2.1. Once the normal is found, it is necessary to identify the surface element $\mathcal{S}_i^{\text{tar}} \in \mathcal{G}_{\text{tar}}$ that is intersected by the line defined by the location of P_i^{proj} and the direction of $\boldsymbol{n}_i^{\text{proj}}$. The element $\mathcal{S}_i^{\text{tar}}$ presents the quadrilateral subsurface on which the point is projected, and once identified, its four nodal points $P_{i,j}^{\text{tar}}$ and respective normal vectors $\boldsymbol{n}_{i,j}^{\text{tar}}$, $j \in \{1,2,3,4\}$ are retrieved. Thus it is also necessary to calculate the normal vector $\boldsymbol{n}_i^{\text{tar}}$ at each point i of the target surface $\mathcal{G}_{\text{tar}}$. In the next step, $P_{i,j}^{\text{tar}}$ and $\boldsymbol{n}_{i,j}^{\text{tar}}$, $j \in \{1,2,3,4\}$ are mapped to the local coordinate system $(\widetilde{x},\widetilde{y},\widetilde{z})$ with the origin at P_i^{proj} and the coordinate axis $\widetilde{z}$ oriented in the direction of $\boldsymbol{n}_i^{\text{proj}}$. The remaining local basis vectors $\widetilde{x}$, $\widetilde{y}$ and the mapping $\mathbb{R}$ are determined using Equations (3) and (4). The position vectors $\widetilde{P}_{i,j}^{\text{tar}}$ and $\widetilde{\boldsymbol{n}}_{i,j}^{\text{tar}}$, $j \in \{1,2,3,4\}$ are thus determined by

$$\widetilde{\boldsymbol{P}}_{i,j}^{\text{tar}} = \mathbb{R}(\boldsymbol{r},\theta)\cdot\left(\boldsymbol{P}_{i,j}^{\text{tar}} - \boldsymbol{P}_i^{\text{proj}}\right), \quad \widetilde{\boldsymbol{n}}_{i,j}^{\text{tar}} = \mathbb{R}(\boldsymbol{r},\theta)\cdot\boldsymbol{n}_{i,j}^{\text{tar}}, \quad j \in \{1,2,3,4\}. \tag{8}$$

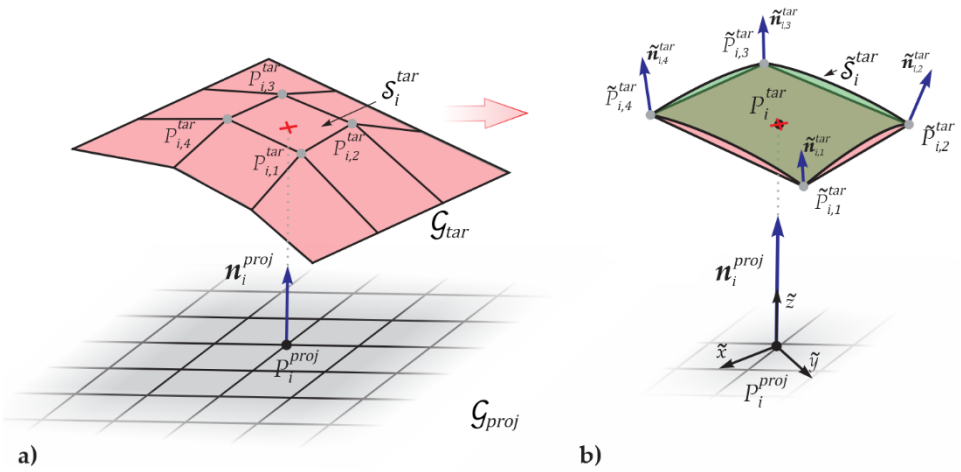

Figure 2. Projection of an arbitrary point $P_i^{\text{proj}} \in \mathcal{G}_{\text{proj}}$ on $\mathcal{G}_{\text{tar}}$ along normal direction: (**a**) identification of the surface element $\mathcal{S}_i^{\text{tar}} \in \mathcal{G}_{\text{tar}}$ that is intersected by the line defined by the location of P_i^{proj} and the direction of $\boldsymbol{n}_i^{\text{proj}}$, (**b**) approximation of $\mathcal{S}_i^{\text{tar}}$ by using the local position vectors $\widetilde{P}_{i,j}^{\text{tar}}$ and the associated normal vectors $\widetilde{\boldsymbol{n}}_{i,j}^{\text{tar}}$ by polynomial surface approximation $\widetilde{S}_i^{\text{tar}}(\widetilde{x},\widetilde{y},\widetilde{z}) = 0$.

Now we can approximate $\mathcal{S}_i^{\text{tar}}$ using the local position vectors $\widetilde{P}_{i,j}^{\text{tar}}$ and the associated normal vectors $\widetilde{\boldsymbol{n}}_{i,j}^{\text{tar}} = \left((\widetilde{n}_{\widetilde{x}})_{i,j}^{\text{tar}}, \left(\widetilde{n}_{\widetilde{y}}\right)_{i,j}^{\text{tar}}, (\widetilde{n}_{\widetilde{z}})_{i,j}^{\text{tar}}\right)$ at four interpolation points. This can be achieved by the functional form:

$$\widetilde{S}_i^{\text{tar}}(\widetilde{x},\widetilde{y},\widetilde{z}) = \widetilde{z} - \left(a_1 + a_2\widetilde{x} + a_3\widetilde{y} + a_4\widetilde{x}\widetilde{y} + a_5\widetilde{x}^2 + a_6\widetilde{y}^2 + a_7\widetilde{x}^2\widetilde{y} + a_8\widetilde{x}\widetilde{y}^2 + a_9\widetilde{x}^2\widetilde{y}^2 + a_{10}\widetilde{x}^3 + a_{11}\widetilde{y}^3 + a_{12}\widetilde{x}^3\widetilde{y}^3\right) = 0, \tag{9}$$

with twelve coefficients a_m, $m \in \{1,2,\ldots,12\}$ to be determined. By requiring that the surface $\widetilde{S}_i^{\text{tar}}(\widetilde{x},\widetilde{y},\widetilde{z}) = 0$ should meet the interpolation requirements at $\widetilde{P}_{i,j}^{\text{tar}}$, $j \in \{1,2,3,4\}$, the following system of linear equations can be set up:

$$\widetilde{S}_i^{\text{tar}}(\widetilde{x}_j,\widetilde{y}_j,\widetilde{z}_j) = 0, \quad \frac{\partial \widetilde{S}_i^{\text{tar}}}{\partial \widetilde{x}}(\widetilde{x}_j,\widetilde{y}_j,\widetilde{z}_j) = \frac{(\widetilde{n}_x)_{i,j}^{\text{tar}}}{(\widetilde{n}_{\widetilde{z}})_{i,j}^{\text{tar}}}, \quad \frac{\partial \widetilde{S}_i^{\text{tar}}}{\partial \widetilde{y}}(\widetilde{x}_j,\widetilde{y}_j,\widetilde{z}_j) = \frac{\left(\widetilde{n}_y\right)_{i,j}^{\text{tar}}}{(\widetilde{n}_{\widetilde{z}})_{i,j}^{\text{tar}}}, \quad j \in \{1,2,3,4\}, \tag{10}$$

whose solution yields the values of the coefficients a_m. Here it should be emphasized that using normal vectors $\widetilde{\boldsymbol{n}}_{i,j}^{\text{tar}}$ and points coordinates $\widetilde{P}_{i,j}^{\text{tar}}$ improves the description of the surface geometry as the polynomial of higher order can be used for the interpolation. Continuity C^1 can be achieved if rectangular sub-surfaces are used to describe $\mathcal{G}_{\text{tar}}$ topology.

Considering that the origin of the local coordinate system is at the point P_i^{proj}, the distance between point P_i^{proj} and its normal projection on the surface $\mathcal{S}_i^{\text{tar}}$ can be retrieved by the value of $\widetilde{z}$ coordinate in the surface formulation $\widetilde{S}_i^{\text{tar}}\left(\widetilde{x}_j, \widetilde{y}_j, \widetilde{z}_j\right) = 0$ when setting $\widetilde{x} = \widetilde{y} = 0$. This yields the distance $d_i = a_1$, and the vector from point P_i^{proj} to its normal projection on the surface $\mathcal{S}_i^{\text{tar}}$, say P_i^{tar}, is given as $\boldsymbol{d}_i = d_i \boldsymbol{n}_i^{\text{proj}}$. Finally, the point topology $\mathcal{G}_{\text{proj}}$ mapped to surface point topology $\mathcal{G}_{\text{tar}}$ for an arbitrary point P_i^{proj} is given by

$$\boldsymbol{P}_i^{\text{tar}} = \boldsymbol{P}_i^{\text{proj}} + \boldsymbol{d}_i. \tag{11}$$

In conclusion, it should be emphasized that there are two major outcomes of the projection mapping procedure. The first one is the distance between the point under consideration on $\mathcal{G}_{\text{proj}}$ and its image on $\mathcal{G}_{\text{tar}}$. For example, this information is essential for the algorithm to decide when the simulated product geometry $\mathcal{G}_{\text{sim,m}}$ as a result of tool and blank optimization achieves the desired product geometry $\mathcal{G}_{\text{ref}}$. The second outcome is the mapping procedure, which is essential for establishing a tool correction procedure.

4. Methodology for the Simultaneous Optimization of Blank Shape and Forming Tool Design

This section presents the method for the simultaneous forming tool design and blank shape optimization in three-dimensional sheet metal forming operations. The basic logic behind the procedure is to sequentially update the forming tool geometry and blank edge geometry to match the desired geometry as specified by the product designer. This can be achieved by accomplishing several activities (blocks), where each activity requires several steps to be taken (c.f. Figure 3). A detailed description of each activity is given below.

The process begins with the desired product shape $\mathcal{G}_{\text{ref}}$. The tool and blank correction rely upon an adequate computer simulation of the sheet metal forming process, which is followed by a degree of springback that occurs after tool removal. To simulate the process, forming process parameters, such as tool and blank geometry, tool kinematics, friction conditions, and blank-holder forces, must also be provided (Block 1). For the procedure, it is essential that the initial blank and tool geometry approximations, $\mathcal{G}_{\text{bl}}^{(0)}$ and $\mathcal{G}_{\text{tool}}^{(0)}$, are provided before the optimization process. The latter can be considered equal to the desired product geometry as $\mathcal{G}_{\text{tool}}^{(0)} = \mathcal{G}_{\text{ref}}$, whereas the initial blank shape approximation can be chosen from experience (Block 2).

After the aforementioned initialization steps (Block 1 and Block 2), the iterative optimization procedure takes place (Block 3). The first activity in the kth iteration of the optimization is related to the FEM simulation of the forming process, followed by the springback (Block 4). In this particular case it is worth noting that in the FEM simulation, the sheet metal is realized as a shell model with quadrilateral finite element mesh discretization, whereas the tool and reference geometry is approximated using quadrilateral discrete rigid elements. The outcome of the simulation is a simulated product geometry $\mathcal{G}_{\text{sim}}^{(k)}$ (or actual geometry), which is an approximation of the desired geometry of the product $\mathcal{G}_{\text{ref}}$.

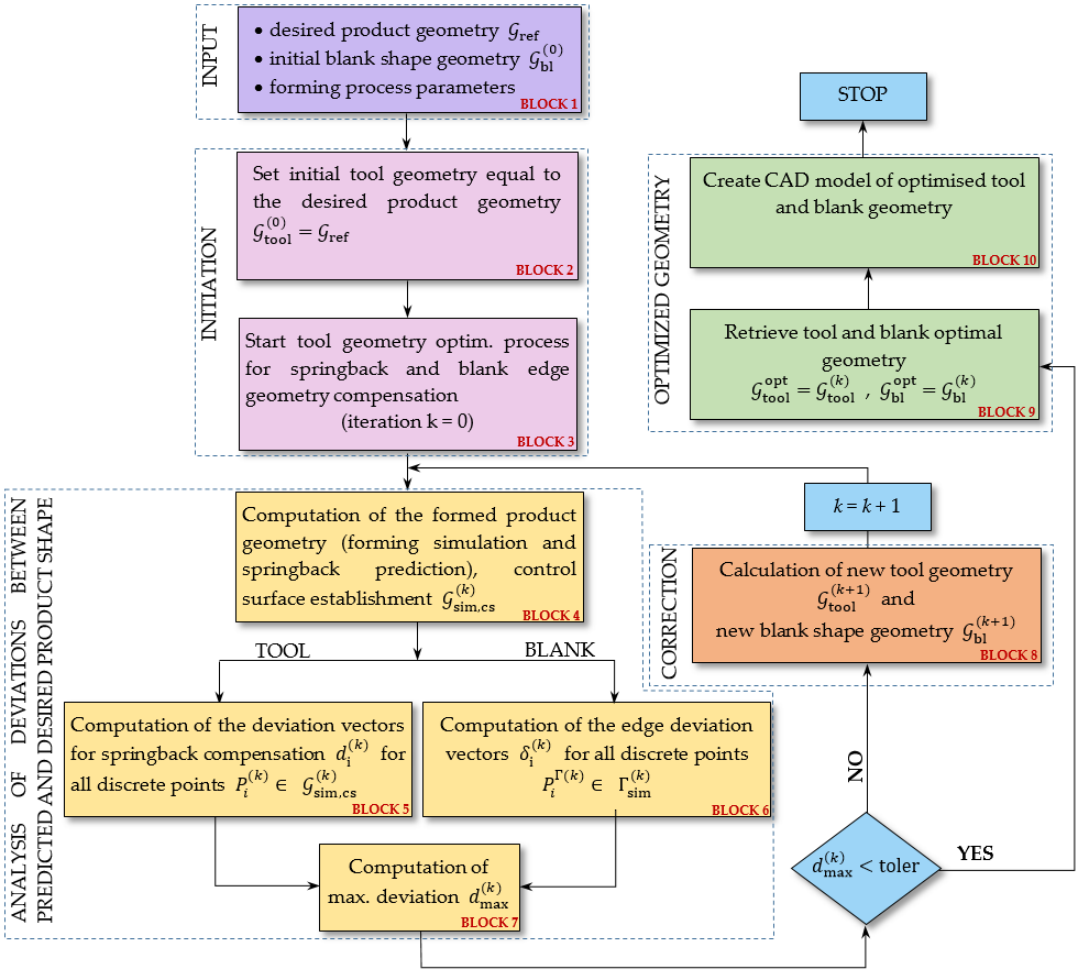

Figure 3. Flowchart of the iterative optimization procedure summarized in the flowchart blocks.

Before taking any further steps, we establish the simulated product topology on the product mid-surface $\mathcal{G}_{sim,m}^{(k)}$ ($= \mathcal{G}_{sim}^{(k)}$ for shell FE model), and the topology on the control (contact) surface, denoted as $\mathcal{G}_{sim,cs}^{(k)} = \mathcal{G}_{sim,m}^{(k)} \pm t_{sim}^{(k)}/2$ (the sign depends on the contact direction). The process is repeated for the desired product geometry $\mathcal{G}_{ref}$, where the desired product thickness t_{ref} is taken into account for $\mathcal{G}_{ref,cs} = \mathcal{G}_{ref,m} \pm t_{ref}/2$, $\mathcal{G}_{ref,m} = \mathcal{G}_{ref}$.

To quantify the mismatch between the simulated geometry $\mathcal{G}_{sim,cs}^{(k)}$ and the desired geometry $\mathcal{G}_{ref,cs}$ a deviation should be evaluated (Block 5). This is achieved by the procedure established in Section 3.3, where we calculate the projection distance $d_i^{(k)}$ from an arbitrary point i associated with the FE mesh on the control surface of the simulated product geometry, say $P_i^{(k)}$, along with its normal projection along $\boldsymbol{n}_i^{(k)}$ to a point on the desired product surface $\mathcal{G}_{ref,cs}$. Again, it is worth noting that in the FE model, the product geometry is characterized by its mid-surface $\mathcal{G}_{sim,m}^{(k)}$ and its thickness $t_i^{(k)}$, meaning that thickness should be taken into account when constructing the control surface topology $\mathcal{G}_{sim,cs}^{(k)}$ and the associated desired surface topology $\mathcal{G}_{ref,cs}$. This way, control of the simulated product thickness $t_i^{(k)}$ is established during the optimisation process.

While the normal projection distance $d_i^{(k)}$ at each point of the simulated surface $\mathcal{G}_{sim,cs}^{(k)}$ indicates the predominant springback and thickness reduction amount to be compensated by the tool geometry $\mathcal{G}_{tool}^{(k)}$, the deviation of the simulated surface edge geometry $\Gamma_{sim}^{(k)}$ from the desired edge geometry Γ_{ref}, say $\delta_i^{(k)}$ is mainly due to sheet blank-holding and drawing conditions. This deviation can be reduced by proper blank shape design characterized by

its edge $\Gamma_{\mathrm{bl}}^{(k)}$. In contrast to $d_i^{(k)}$, which is the projection distance in the normal direction $\boldsymbol{n}_i^{(k)}$ of the $\mathcal{G}_{\mathrm{sim,cs}}^{(k)}$ to the $\mathcal{G}_{\mathrm{ref,cs}}$, $\delta_i^{(k)}$ can be characterized as the distance in edge normal direction $\boldsymbol{n}_i^{\Gamma(\mathrm{k})}$ at an arbitrary point $P_i^{\Gamma(k)}$ on edge $\Gamma_{\mathrm{sim}}^{(k)}$. This is addressed in Block 6. To obtain its value, four steps are necessary. In the first step, we construct edge normals $\boldsymbol{n}_i^{\Gamma(\mathrm{k})}$ for all the edge points $P_i^{\Gamma(k)}$ of the edge point topology $\Gamma_{\mathrm{sim}}^{(k)}$. This is accomplished according to the procedure described in Section 3.2.2. Following the same procedure, in the second step, we also construct edge normals $\boldsymbol{n}_i^{\mathrm{ref},\Gamma}$ for all the edge points of the desired point topology $\mathcal{G}_{\mathrm{ref,m}}$. In the third and crucial step, we construct an auxiliary surface point topology, say $\mathcal{G}_{\mathrm{aux}}$, perpendicular to the edge $\Gamma_{\mathrm{ref}} \in \mathcal{G}_{\mathrm{ref,m}}$, by using a set of edge points $P_i^{\mathrm{ref},\Gamma}$ and new points P_i^{aux}, dislocated from $P_i^{\mathrm{ref},\Gamma}$ in the normal direction $\boldsymbol{n}_i^{\mathrm{ref}}$ of $\mathcal{G}_{\mathrm{ref,m}}$ for a predefined distance. The constructed auxiliary surface $\mathcal{G}_{\mathrm{aux}}$ is presented in Figure 4a. In the last step, we project all edge points $P_i^{\Gamma(k)} \in \Gamma_{\mathrm{sim}}^{(k)}$ to the $\mathcal{G}_{\mathrm{aux}}$ along $\boldsymbol{n}_i^{\Gamma(k)}$ and calculate the projection distance $\delta_i^{(k)}$ according to the procedure established in Section 3.3. A graphical presentation of this step is presented in Figure 4b.

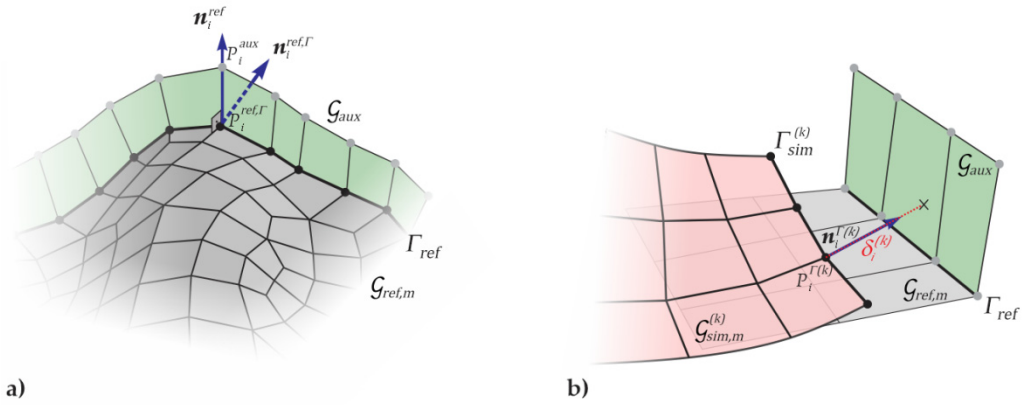

Figure 4. Procedure for the calculation of $\delta_i^{(k)}$: (**a**) construction of an auxiliary surface $\mathcal{G}_{\mathrm{aux}}$ perpendicular to the edge $\Gamma_{\mathrm{ref}} \in \mathcal{G}_{\mathrm{ref,m}}$, (**b**) calculation of the projection distance $\delta_i^{(k)}$ according to the established procedure.

Once a set of distances, $\left\{d_i^{(k)}\right\}$ and $\left\{\delta_i^{(k)}\right\}$, associated with the surface and edge point topology $\mathcal{G}_{\mathrm{sim,cs}}^{(k)}$ and $\Gamma_{\mathrm{sim}}^{(k)}$, are calculated, their maximum value $d_{\mathrm{max}}^{(k)} = \max\left(\left\{d_i^{(k)}\right\}, \left\{\delta_i^{(k)}\right\}\right)$ can be found (Block 7). If the value is within the acceptable tolerance, the optimal tool geometry $\mathcal{G}_{\mathrm{tool}}^{\mathrm{opt}} = \mathcal{G}_{\mathrm{tool}}^{(k)}$ and optimal blank shape geometry $\mathcal{G}_{\mathrm{bl}}^{\mathrm{opt}} = \mathcal{G}_{\mathrm{bl}}^{(k)}$ have been attained (Block 9). In this case, both geometries can be exported from the FEM environment to create a CAD model for further tool and blank fabrication (Blank 10). If $d_{\mathrm{max}}^{(k)}$ does not fall within the acceptable tolerance, the tool geometry $\mathcal{G}_{\mathrm{tool}}^{(k)}$ and blank shape $\Gamma_{\mathrm{bl}}^{(k)}$ are adjusted. This is achieved by a procedure schematically shown in Block 8, where the deviations $d_i^{(k)}$ and $\delta_i^{(k)}$ play a crucial role. Both the tool and the blank adjustment procedures are presented in the following subsections and once the geometries are updated, a new iteration takes place.

4.1. Tool Geometry Adjustment

The basic idea behind the tool adjustment is that the calculated deviations $d_i^{(k)}$ at points $P_i^{(k)} \in \mathcal{G}_{\mathrm{sim,cs}}^{(k)}$ are used for tool correction. Because the simulated product control surface point topology $\mathcal{G}_{\mathrm{sim,cs}}^{(k)}$ and tool surface point topology $\mathcal{G}_{\mathrm{tool}}^{(k)}$ generally have different topological structure, and because it is practically impossible to predict which point $P_i^{(k)} \in \mathcal{G}_{\mathrm{sim,cs}}^{(k)}$ interacts with an associated point $T_i^{(k)} \in \mathcal{G}_{\mathrm{tool}}^{(k)}$, some mapping procedures need to be applied to address these issues.

In the first step, we construct an auxiliary surface, say $\mathcal{G}_{\mathrm{A}}^{(k)}$, by mapping the simulated product control surface point topology $\mathcal{G}'^{(k)}_{\mathrm{sim,cs}}$ to the tool surface point topology $\mathcal{G}_{\mathrm{tool}}^{(k)}$ to match their topological structures. To locate which point $P_i^{(k)} \in \mathcal{G}_{\mathrm{sim,cs}}^{(k)}$ interacts with an associated point on $\mathcal{G}_{\mathrm{tool}}^{(k)}$, we consider the simulated product control surface point topology before the springback simulation, denoted as $\mathcal{G}'^{(k)}_{\mathrm{sim,cs}}$. The mapping is performed by employing the procedure established in Section 3.3, where the projected surface is $\mathcal{G}'^{(k)}_{\mathrm{sim,cs}}$ and target surface $\mathcal{G}_{\mathrm{tool}}^{(k)}$.

In the second step, we apply the adjustment to $\mathcal{G}_{\mathrm{A}}^{(k)}$ by using calculated the deviations $d_i^{(k)}$ between the $\mathcal{G}_{\mathrm{sim,cs}}^{(k)}$ and $\mathcal{G}_{\mathrm{ref,cs}}$. We construct a new auxiliary surface, say $\mathcal{G}_{\mathrm{B}}^{(k)}$, where an arbitrary point $P_{\mathrm{A},i}^{(k)} \in \mathcal{G}_{\mathrm{A}}^{(k)}$ is mapped to point $P_{\mathrm{B},i}^{(k)} \in \mathcal{G}_{\mathrm{B}}^{(k)}$ as

$$\boldsymbol{P}_{\mathrm{B},i}^{(k)} = \boldsymbol{P}_{\mathrm{A},i}^{(k)} + \left(\boldsymbol{d}_i^{(k)} \cdot \boldsymbol{n}_{\mathrm{A},i}^{(k)}\right) \boldsymbol{n}_{\mathrm{A},i}^{(k)}. \tag{12}$$

In this equation, the $P_{\mathrm{A},i}^{(k)}$ and $P_{\mathrm{B},i}^{(k)}$ presents the location vector of $P_{\mathrm{A},i}^{(k)}$ and $P_{\mathrm{B},i}^{(k)}$, $\boldsymbol{n}_{\mathrm{A},i}^{(k)}$ the surface normal vector at $P_{\mathrm{A},i}^{(k)}$ according to Section 3.2.1 and $\boldsymbol{d}_i^{(k)} = d_i^{(k)} \boldsymbol{n}_i^{(k)}$, where $\boldsymbol{n}_i^{(k)}$ is the surface normal vector at $P_i^{(k)} \in \mathcal{G}_{\mathrm{sim,cs}}^{(k)}$. However, it should be noted that the scalar product is used because only a normal component of $\boldsymbol{d}_i^{(k)}$ to $\boldsymbol{n}_{\mathrm{A},i}^{(k)}$ contributes to tool adjustment.

Finally, in the last step, the tool surface point topology $\mathcal{G}_{\mathrm{tool}}^{(k)}$ is projected to the auxiliary surface $\mathcal{G}_{\mathrm{B}}^{(k)}$ by the procedure described in Section 3.3, where the projected surface is $\mathcal{G}_{\mathrm{tool}}^{(k)}$ and the target surface is $\mathcal{G}_{\mathrm{B}}^{(k)}$. As result, the adjusted tool surface point topology $\mathcal{G}_{\mathrm{tool}}^{(k+1)}$ is obtained.

4.2. Blank Shape Adjustment

Blank edge geometry $\Gamma_{\mathrm{bl}}^{(k)} \in \mathcal{G}_{\mathrm{bl,m}}^{(k)}$ is adjusted based on the calculated edge deviations $\delta_i^{(k)}$ between the simulated surface edge geometry $\Gamma_{\mathrm{sim}}^{(k)} \in \mathcal{G}_{\mathrm{sim,m}}^{(k)}$ and the desired edge geometry $\Gamma_{\mathrm{ref}} \in \mathcal{G}_{\mathrm{ref,m}}$. The blank geometry is adjusted in three steps as follows:

In the first step the blank's edge normals $\boldsymbol{n}_{\mathrm{bl},i}^{\Gamma(k)}$ at each edge point $P_{\mathrm{bl},i}^{\Gamma(k)}$ of the $\Gamma_{\mathrm{bl}}^{(k)}$ are calculated using the procedure described in Section 3.2.2. Once the normals are established, the updated edge point topology $\Gamma_{\mathrm{bl}}^{(k+1)}$ is constructed in the second step:

$$\boldsymbol{P}_{\mathrm{bl},i}^{\Gamma(k+1)} = \boldsymbol{P}_{\mathrm{bl},i}^{\Gamma(k)} + \delta_i^{(k)} \cdot \boldsymbol{n}_{\mathrm{bl},i}^{\Gamma(\mathrm{k})}, \tag{13}$$

where $P_{\mathrm{bl},i}^{\Gamma(k)}$ presents an edge point position vector (edge point coordinates) from the beginning of the k-th iteration, and $P_{\mathrm{bl},i}^{\Gamma(k+1)}$ an edge point position vector at the end of the iteration.

The last step yields the blank geometry, where only the blank edge point topology $\Gamma_{\mathrm{bl}}^{(k+1)}$ is adjusted. Interior points of the blank surface topology, say $\mathcal{G}_{\mathrm{bl,int}}^{(k)} = \mathcal{G}_{\mathrm{bl,m}}^{(k)} \setminus \Gamma_{\mathrm{bl}}^{(k)}$, remain unadjusted, which could result in poor FE mesh quality. To resolve this issue, we map interior points of $\mathcal{G}_{\mathrm{bl,m}}^{(k)}$ proportionally with the distance from the adjusted edge $\Gamma_{\mathrm{bl}}^{(k+1)}$. Although this seems a relatively difficult task, we map interior points by simulating a separate elastic boundary problem, where the blank geometry $\mathcal{G}_{\mathrm{bl,m}}^{(k)}$ is subjected to displacement-driven boundary conditions with the edge displacement at an arbitrary point $P_{\mathrm{bl},i}^{\Gamma(k)}$ set as $\delta_i^{(k)} \cdot \boldsymbol{n}_{\mathrm{bl},i}^{\Gamma(\mathrm{k})}$. Finally, the geometry of the blank shape at the loaded state is retrieved as $\mathcal{G}_{\mathrm{bl,m}}^{(k+1)}$.

5. Results of Forming Tool and Blank Shape Design Optimization

5.1. Forming Process Simulation and Optimization Procedure

In this section, the presented methodology for simultaneous tool and blank design optimization is applied to an automotive part made of *complex-phase advanced high strength steel* HDT 760C sheet, which tends to exhibit a considerable amount of springback after tool removal, owing to the high ratio of yield stress to tensile strength. Since these steels have high crash energy absorption, they are recommended in lightweight automotive applications such as stiffeners, sills, door impact bars, seat mounting rails, and automotive chassis components. The fine microstructure of the sheet leads to high formability of punched edges while maintaining good bending properties. According to EN 10346, its chemical composition is 0.18% C, 2.5 Mn, 1.0% Si, 1.0% Cr+Mo, 0.25% Nb+Ti, 0.20% V, 0.005% B, 0.015–2.00% Al, 0.08% P, 0.015% S, and balance Fe (max wt.%).

The mechanical properties of the sheet material are given in Table 1. Since the plastic anisotropy of the analyzed steel sheet is mild, we assume that the material response is isotropic and that during the forming process no significant reverse bending occurs, which means kinematic hardening effects can be neglected. The assumed hardening relation closely follows Ludwik's hardening law by $\left(\varepsilon_{eq}^{pl}\right) = \sigma_0 + H\left(\varepsilon_{eq}^{pl}\right)^n$, where the parameters are obtained by nonlinear regression.

Table 1. Elastic and plastic parameters of HDT760C calculated from the uniaxial tensile test data.

Isotropic Elasticity (Hooke's Law)		Isotropic Hardening (Ludwig's Law)	
E	201 GPa	σ_0	620.6 MPa
ν	0.3	H	504.3 MPa
		n	0.217

In the forming process under consideration, the final product is produced in two consecutive forming steps, each of them using different tool set-up geometries as presented in Figure 5. In the first forming step, the blank is formed into a semi-product; in the second step, this is followed by forming into the final shape. In both steps, the sheet is held in place with a blank holding force of 24 kN. The workpiece is passed from one forming operation to the other with the help of a strip connected to the workpiece; after the trimming phase, this is scrapped. The final product should fulfil the costumer's specifications, showing no surface defects (no tearing, wrinkling, or thinning) and fulfilling the specified geometric tolerances (surface and edge deviations less than 0.5 or 1.0 mm, respectively).

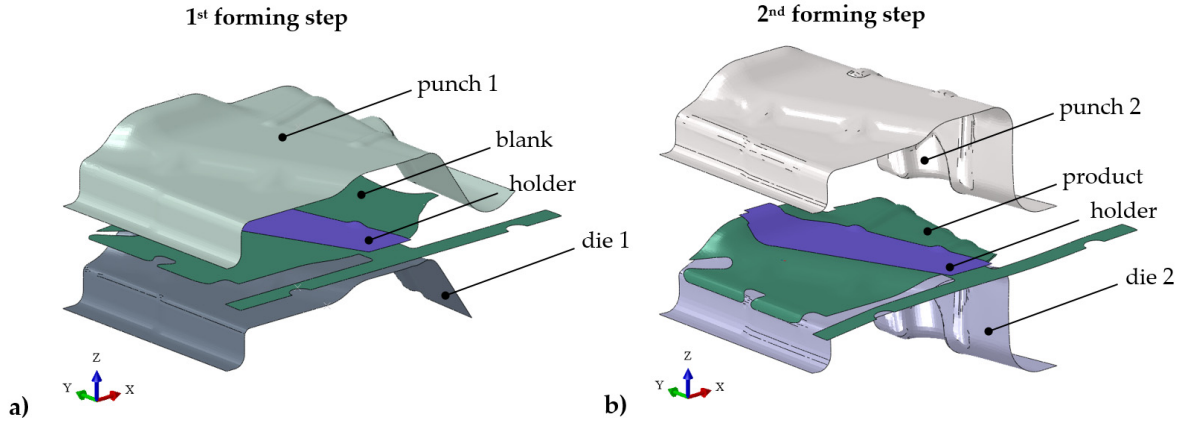

Figure 5. Consecutive production stages: (**a**) first forming step, (**b**) second forming step. In the numerical simulation, each step consists of a loading and an unloading stage associated with the forming and relaxation process. Before the second relaxation stage, a trimming operation is performed.

A numerical simulation of the complete manufacturing process is conducted in the ABAQUS/Explicit and ABAQUS/Standard FEM environments. Both steps of the process consist of a loading stage and an unloading stage, which are associated with irreversible plastic deformation and elastic relaxation. Before loading is applied, the blank or semi-product is held in position using a holder which, to a certain extent, also serves as forming tool (see holder geometry in Figure 5a). The blank-holding stage and the forming operation are simulated in ABAQUS/Explicit, while the unloading and springback associated with the elastic relaxation stage is simulated in ABAQUS/Standard. Trimming operation is conducted before elastic relaxation in the second forming step.

The forming of the blank into the product is carried out using different tool set-ups for each forming phase (c.f. Figure 5). The clearance between the die1/die2 and punch1/punch2 is set to a constant value of 2.2 mm. Both tool set-ups are assumed to be rigid and modelled using discrete rigid surface geometry. Quadrilateral FE mesh using R3D4 finite elements is adopted for the surface description. The sheet metal is modelled as a thin shell meshed with quadrilateral finite elements (S4 elements). Seven integration points distributed evenly across the shell thickness ($t = 2$ mm) are considered in order to take the strain–stress state evolution into account. The characteristic size of the shell and rigid finite elements is 2.5 mm and 3.0 mm, respectively. Tool–sheet contact interaction is modelled using a penalty contact algorithm. Due to contact pressure, stress state, lubrication, and sliding velocity variation at different contact regions, the value of friction coefficient generally varies significantly at different locations of the tools [54]. In our case, we simplified friction modelling by assuming Coulomb's law, where the coefficient of friction is set equal to 0.12 [55].

On one hand, the applied tool set-up boundary conditions are directly associated with the tool kinematics. On the other hand, the workpiece conditions are applied to the connected strip, which is fixed in all directions. Once the strip is trimmed and the workpiece is load-free, an arbitrary node on the workpiece can be fixed to simulate the elastic relaxation and the final self-equilibrium state.

With the FEM model established, the optimization of the tool and blank edge geometry takes place. Since the forming process is conducted in two forming steps, both tool set-ups could be optimized to achieve the desired product geometry. However, this turned out to be redundant in the analyzed case—the optimized workpiece geometry can be achieved by adjusting only the punch and the die for the second forming step. Moreover, in accordance with the costumer's specifications, the surface area in contact with the holder was not subject to the surface optimization procedure.

Determination of the optimal tool and blank geometry is carried out according to the procedure described in Section 4. In the procedure, an initial die and punch geometry is set equivalent to the desired product geometry, taking into account the sheet thickness and clearance. The initial blank geometry is determined empirically and is presented in Figure 6a. During the iteration process, the punch, the die, and the blank geometry are successively adjusted using deviations between the desired product geometry and the simulated geometry. The iterative procedure is continued until the desired product shape (Figure 6b) is achieved within a prescribed tolerance.

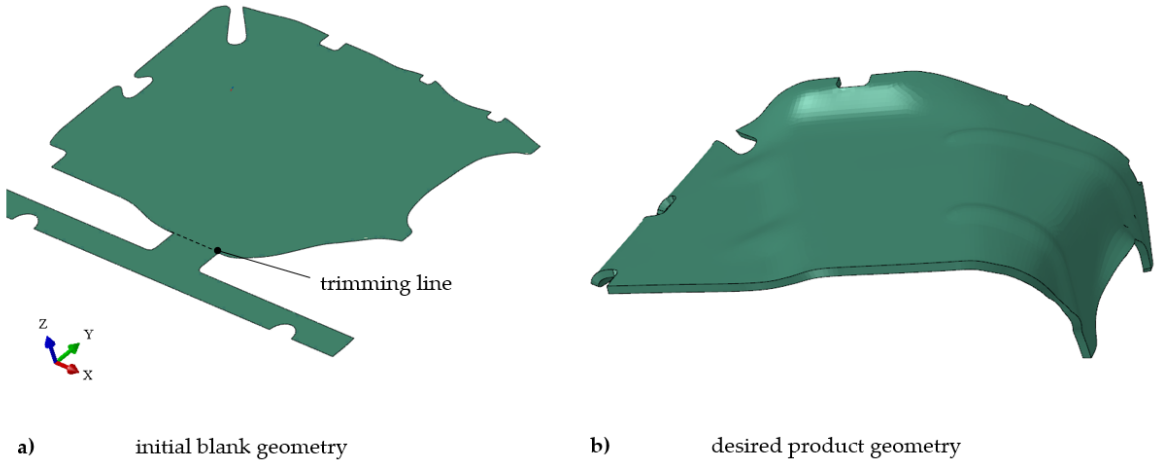

Figure 6. Sheet metal geometries: (**a**) blank initial geometry, (**b**) desired product geometry.

5.2. Results

In the following section, we present the results of the optimization procedure, where the results refer to the forming process with the initial and the optimized tool and blank designs. Product surface and edge deviations calculated from the initial and the optimized tool geometry are both presented in Figure 7. The left column presents the product edge geometry deviations from the desired shape prior (Figure 7a) and after (Figure 7c) the optimization takes place. The right column presents the product surface geometry deviations from the desired shape, once again before (Figure 7b) and after (Figure 7d) springback compensation. While the product geometry calculated from the initial blank and tool geometry results in quite high deviations from the desired shape (about 3 mm in both cases), the deviation is substantially reduced after optimization. In this case, the edge and surface deviations are below 0.15 mm and 0.5 mm, respectively, meaning that our primary target is achieved. The deviations in Figure 7d that are above 0.5 mm occur in the region not subjected to the optimization procedure, in accordance with the costumer's specifications. It should be emphasized that for the particular sheet material, springback compensation is particularly challenging, owing to its high values, presented in Figure 8a. As expected, the springback is highest at the locations most distant from the nearest bending radius. Most surprisingly, when comparing Figure 8a with Figure 7d, it can be observed that this springback is successfully compensated to the resulting deviation under 0.2 mm. On the other hand, using the initial tool design (Figure 7b) the springback directly manifests itself in surface deviation.

The iteration process performed according to the flow chart given in Figure 3 is convergent, with the optimal forming tool and blank edge geometry achieved iteratively. Figure 9 shows the convergence of the proposed method. In this particular case, it can be observed that convergence is achieved in several iterations. Moreover, the method converges in a stable way, without any oscillations, which is significant in the case of sheet materials prone to large springback amounts.

Based on the results of the optimization procedure, the optimal tool and blank geometries were exported to the CAD environment. The individual tool parts and blank shape were produced and the forming process conducted.

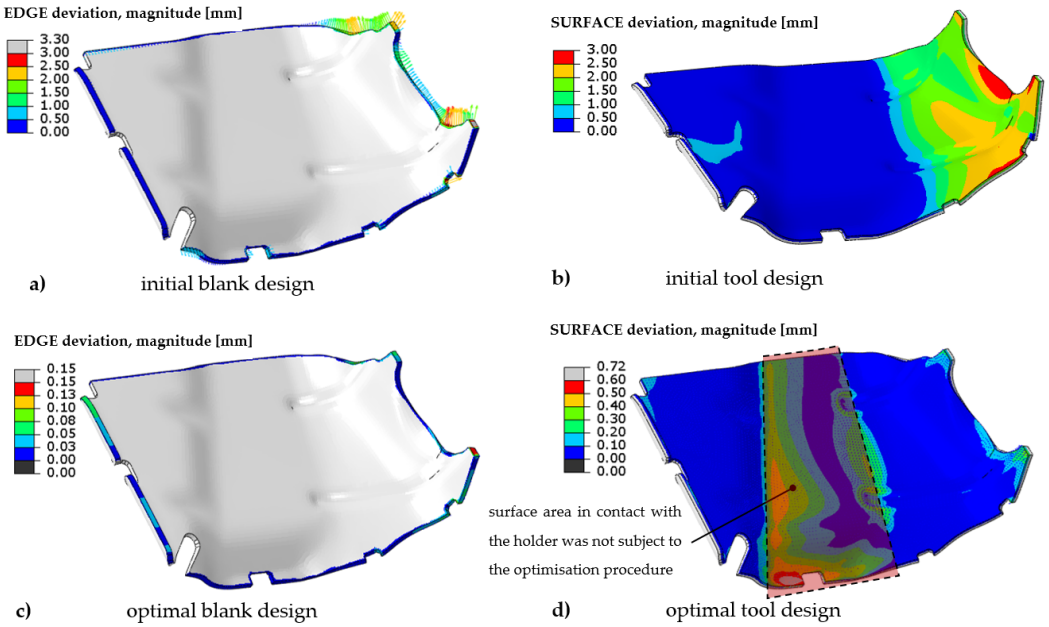

Figure 7. Calculated product surface and edge deviations from desired geometry: (**a**) edge deviations using initial blank geometry, (**b**) surface deviations using initial tool geometry, (**c**) edge deviations using optimal blank geometry, (**d**) surface deviations using optimal tool geometry.

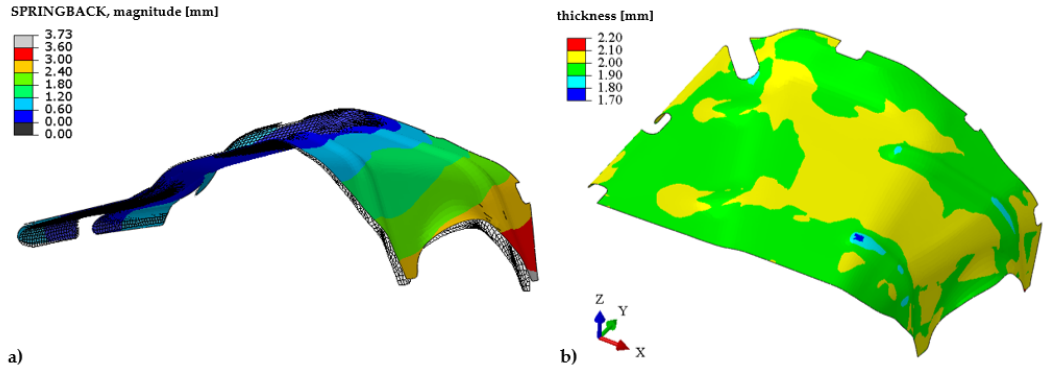

Figure 8. Results of the optimized product simulation: (**a**) compensated springback amount, (**b**) the final product thickness without the presence of thinning.

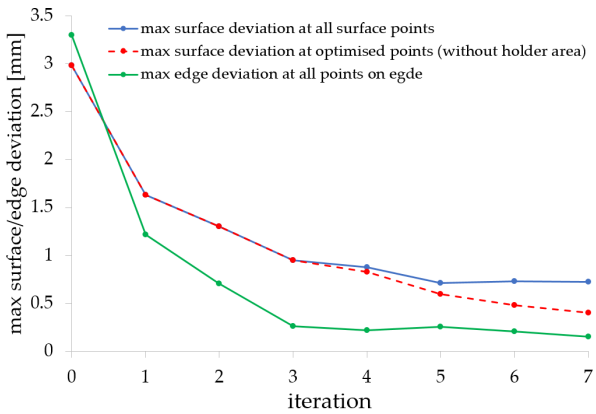

Figure 9. The convergence of the optimization method: (**blue**) maximum surface deviation calculated from deviations at all surface points (including blank holder contact surface area), (**red**) maximum surface deviation calculated from deviations at optimized surface points (without blank holder contact surface area), (**green**) maximum edge deviations calculated from all edge deviations.

5.3. Experimental Verification

Finally, the developed optimization methodology is verified by forming the actual product. As per customer specifications, the measured edge and surface deviations should be smaller than 1.0 mm and 0.5 mm, respectively. Figure 10 shows the measuring locations of the surface (Figure 10a) and the edge (Figure 10b) deviations. The locations on the surface are selected in the region which is prone to significant deviations due to springback. The results are presented in Table 2.

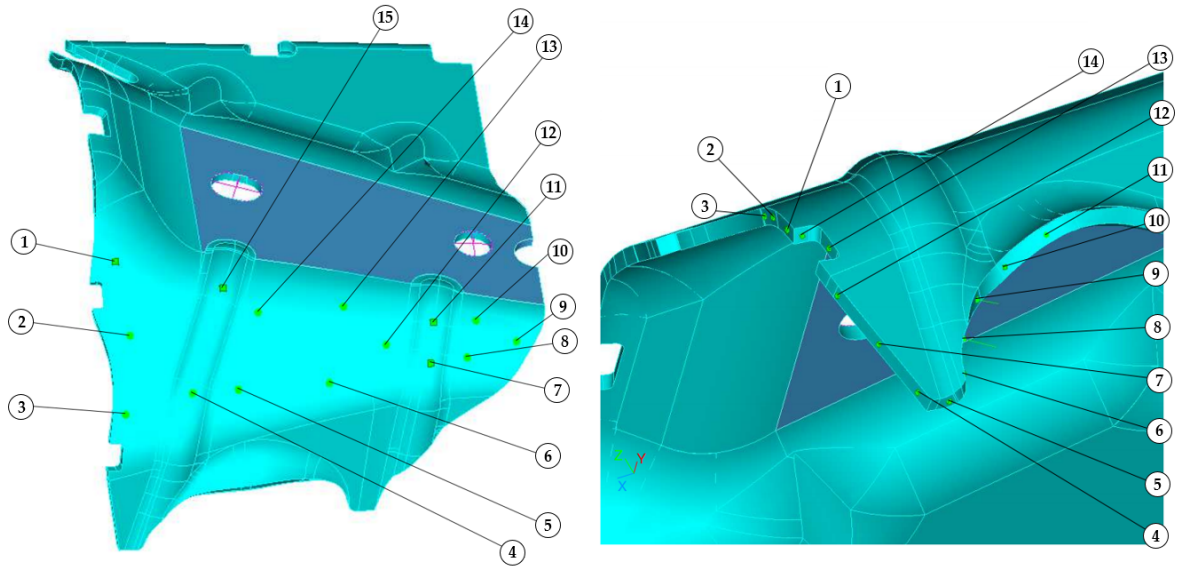

Figure 10. Measured deviations the final product geometry produced by optimized tool geometry in the forming step 2: (**a**) surface deviations, (**b**) edge deviations. Number in a capture represents the surface or edge acquisition point, where the deviation from its optimal shape is measured. The values of deviations are specified in Table 2.

Table 2. Measured deviations of the final product geometry produced by the optimized tool geometry. The location of the measuring points is denoted in Figure 10.

Surface Deviations		Edge Deviations	
Location	**(mm)**	**Location**	**(mm)**
1	0.21	1	0.07
2	0.24	2	0.02
3	0.47	3	0.00
4	0.16	4	0.32
5	0.48	5	0.71
6	0.46	6	0.01
7	0.03	7	0.08
8	0.14	8	0.39
9	0.16	9	0.28
10	0.01	10	0.25
11	0.10	11	0.02
12	0.37	12	0.08
13	0.09	13	0.11
14	0.09	14	0.15
15	0.22	-	-

Table 2 illustrates that the measured deviations are below the required values. It should be noted that the predicted values generally follow the measured ones, with few exceptions (e.g., surface points 3,5,6,12), where the measured deviation is greater than the predicted one. In both cases, however, the improvement in the product geometry

is not as large as predicted by the optimization procedure and corresponding computer simulations. Differences may arise due to many numerical and experimental factors, suspecting tool manufacturing process, surface roughness quality, tool–sheet simulation contact properties, friction properties, forming process and material modelling, deviations measuring technique, etc. Additional uncertainties are introduced by using two forming steps. Nevertheless, the optimization method succeeds in predicting the forming tool and blank geometry such that the customer's specifications are achieved.

6. Conclusions

In this paper, we present a numerical method for the compensation of springback, thinning, and blank edge geometry which results in the simultaneous optimization of the blank shape and forming tool geometry. Based on our previous works, the proposed iterative procedure is developed by integrating the springback (and thinning) compensation algorithm [35,36] and the blank edge geometry correction algorithm [52] into one unified algorithm. To the best of the authors' knowledge, no study has yet comprehensively considered all these phenomena; this thus represents the main novelty of this paper.

The proposed algorithm is capable of optimizing the blank shape and the forming tool geometry in three-dimensional sheet metal forming operations. The algorithm is demonstrated on a complex-phase advanced high strength steel sheet automobile product, which, due to the high ratio of yield stress to tensile strength, is prone to a considerable amount of springback after tool removal. As presented, the algorithm effectively compensates for the springback, thickness reduction, and product edge deviations in seven iterations. As shown, during the convergence process, no oscillations occur and maximum surface and edge deviations are reduced from 3 mm to 0.4 and 0.15 mm, respectively.

Finally, the predicted tool and blank geometries were produced and implemented in the actual forming process. The results showed that using the optimized tool and blank edge geometries, the customer's specifications in the form of allowable deviations between manufactured and desired product geometries were met. The values allowable deviations were prescribed as 0.5 mm for surface and 1.0 mm for edge deviations whereas the maximum measured surface and edge deviations were 0.48 mm and 0.71 mm, respectively. The main reasons for deviations between the measured and predicted values are mainly due to accuracy of material and process modelling assumptions as well as due to experimental factors, such as tool and product surface measurement.

Finally, the procedure is significant for practical industrial applications. The methodology and the developed software have been introduced in the company's R&D division product development and proven to be successful in practical applications.

Author Contributions: Conceptualization, G.C. and N.M.; methodology, G.C. and N.M; software, G.C.; validation, B.S. and N.M.; formal analysis, G.C.; investigation, G.C. and N.M.; resources, N.M.; data curation, G.C. and B.S.; writing—original draft preparation, B.S.; writing—review and editing, B.S. and N.M.; visualization, B.S.; supervision, N.M.; project administration, N.M.; funding acquisition, N.M. All authors have read and agreed to the published version of the manuscript.

Funding: This research was funded by the Slovenian Research Agency, grant number P2-0263.

Institutional Review Board Statement: Not applicable.

Informed Consent Statement: Not applicable.

Data Availability Statement: The data presented in this study are available on request from the corresponding author. The data are not publicly available due to its privacy.

Acknowledgments: The authors acknowledge the financial support from the Slovenian Research Agency (research core funding No. P2-0263). The authors also thank TPV Automotive d.o.o. for supplying sheet metal product design used in the optimization procedure.

Conflicts of Interest: The authors declare no conflict of interest.

References

1. Caro, L.P.; Odenberger, E.-L.; Schill, M.; Niklasson, F.; Åkerfeldt, P.; Oldenburg, M. Springback prediction and validation in hot forming of a double-curved component in alloy 718. *Int. J. Mater. Form.* **2021**, 1–19. [CrossRef]
2. Menezes, L.; Teodosiu, C. Three-dimensional numerical simulation of the deep-drawing process using solid finite elements. *J. Mater. Process. Technol.* **2000**, *97*, 100–106. [CrossRef]
3. Tekkaya, A.E. State-of-the-art of simulation of sheet metal forming. *J. Mater. Process. Technol.* **2000**, *103*, 14–22. [CrossRef]
4. Pepelnjak, T.; Barišić, B. Computer-assisted engineering determination of the formability limit for thin sheet metals by a modified Marciniak method. *J. Strain Anal. Eng. Des.* **2009**, *44*, 459–472. [CrossRef]
5. Zhu, M.; Lim, Y.C.; Liu, X.; Cai, Z.; Dhawan, S.; Gao, H.; Politis, D.J. Numerical forming limit prediction for the optimisation of initial blank shape in hot stamping of AA7075. *Int. J. Lightweight Mater. Manuf.* **2021**, *4*, 269–280. [CrossRef]
6. Feng, Z.; Champliaud, H.; Sabourin, M.; Morin, S. Optimal blank design based on finite element method for blades of large Francis turbines. *Simul. Model. Pract. Theory* **2013**, *36*, 11–21. [CrossRef]
7. Azaouzi, M.; Naceur, H.; Delaméziere, A.; Batoz, J.; Belouettar, S. An Heuristic Optimization Algorithm for the blank shape design of high precision metallic parts obtained by a particular stamping process. *Finite Elem. Anal. Des.* **2008**, *44*, 842–850. [CrossRef]
8. Mulidrán, P.; Spišák, E.; Tomáš, M.; Slota, J.; Majerníková, J. Numerical Prediction and Reduction of Hat-Shaped Part Springback Made of Dual-Phase AHSS Steel. *Metals* **2020**, *10*, 1119. [CrossRef]
9. Ingarao, G.; Di Lorenzo, R.; Micari, F. Analysis of stamping performances of dual phase steels: A multi-objective approach to reduce springback and thinning failure. *Mater. Des.* **2009**, *30*, 4421–4433. [CrossRef]
10. Cui, X.; Xiao, A.; Du, Z.; Yan, Z.; Yu, H. Springback Reduction of L-Shaped Part Using Magnetic Pulse Forming. *Metals* **2020**, *10*, 390. [CrossRef]
11. Gan, W.; Wagoner, R. Die design method for sheet springback. *Int. J. Mech. Sci.* **2004**, *46*, 1097–1113. [CrossRef]
12. Ma, R.; Wang, C.; Zhai, R.; Zhao, J. An Iterative Compensation Algorithm for Springback Control in Plane Deformation and Its Application. *Chin. J. Mech. Eng.* **2019**, *32*, 28. [CrossRef]
13. Lingbeek, R.; Huétink, J.; Ohnimus, S.; Petzoldt, M.; Weiher, J. The development of a finite elements based springback compensation tool for sheet metal products. *J. Mater. Process. Technol.* **2005**, *169*, 115–125. [CrossRef]
14. Meinders, T.; Burchitz, I.; Bonte, M.; Lingbeek, R. Numerical product design: Springback prediction, compensation and optimization. *Int. J. Mach. Tools Manuf.* **2008**, *48*, 499–514. [CrossRef]
15. Lan, F.; Chen, J.; Lin, J. A method of constructing smooth tool surfaces for FE prediction of springback in sheet metal forming. *J. Mater. Process. Technol.* **2006**, *177*, 382–385. [CrossRef]
16. Lu, B.; Ou, H.; Armstrong, C.; Rennie, A. 3D die shape optimisation for net-shape forging of aerofoil blades. *Mater. Des.* **2009**, *30*, 2490–2500. [CrossRef]
17. Liao, J.; Xue, X.; Lee, M.-G.; Barlat, F.; Grácio, J. On twist springback prediction of asymmetric tube in rotary draw bending with different constitutive models. *Int. J. Mech. Sci.* **2014**, *89*, 311–322. [CrossRef]
18. Yang, X.A.; Ruan, F. A die design method for springback compensation based on displacement adjustment. *Int. J. Mech. Sci.* **2011**, *53*, 399–406. [CrossRef]
19. Gong, Z.; Zhan, Z.; Xu, Z.; Sun, G.; Zheng, G.; Cui, J. Research on the whole tool mesh reconstruction in the process of springback compensation for auto-body panels. *Int. J. Mater. Form.* **2018**, *11*, 77–85. [CrossRef]
20. Livatyali, H.; Ergeldi, M. Design of over-crown in sheet metal stamping using finite element method. *J. Mater. Process. Technol.* **2006**, *173*, 14–20. [CrossRef]
21. Cimolin, F.; Vadori, R.; Canuto, C. Springback compensation in deep drawing applications. *Meccanica* **2008**, *43*, 101–113. [CrossRef]
22. Karafillis, A.; Boyce, M. Tooling design accomodating springback errors. *J. Mater. Process. Technol.* **1992**, *32*, 499–508. [CrossRef]
23. Karafillis, A.P.; Boyce, M.C. Tooling and binder design for sheet metal forming processes compensating springback error. *Int. J. Mach. Tools Manuf.* **1996**, *36*, 503–526. [CrossRef]
24. Cheng, H.S.; Cao, J.; Xia, Z.C. An accelerated springback compensation method. *Int. J. Mech. Sci.* **2007**, *49*, 267–279. [CrossRef]
25. Bahloul, R.; Ben-Elechi, S.; Potiron, A. Optimisation of springback predicted by experimental and numerical approach by using response surface methodology. *J. Mater. Process. Technol.* **2006**, *173*, 101–110. [CrossRef]
26. Shi, X.; Chen, J.; Peng, Y.; Ruan, X. A new approach of die shape optimization for sheet metal forming processes. *J. Mater. Process. Technol.* **2004**, *152*, 35–42. [CrossRef]
27. Palmieri, M.; Lorusso, V.; Tricarico, L. Robust Optimization and Kriging Metamodeling of Deep-Drawing Process to Obtain a Regulation Curve of Blank Holder Force. *Metals* **2021**, *11*, 319. [CrossRef]
28. Chen, C.; Liang, J.; Teng, F.; Li, Y.; Liang, C. Research on springback compensation method of 3D flexible stretch bending of multi-point roller dies. *Int. J. Adv. Manuf. Technol.* **2021**, *112*, 563–575. [CrossRef]
29. Zhang, S.; Fu, M.; Wang, Z.; Fang, D.; Lin, W.; Zhou, H. Springback prediction model and its compensation method for the variable curvature metal tube bending forming. *Int. J. Adv. Manuf. Technol.* **2021**, *112*, 3151–3165. [CrossRef]
30. Wei, L.; Yuying, Y.; Zhongwen, X.; Lihong, Z. Springback control of sheet metal forming based on the response-surface method and multi-objective genetic algorithm. *Mater. Sci. Eng. A* **2009**, *499*, 325–328. [CrossRef]
31. Schenk, O.; Hillmann, M. Optimal design of metal forming die surfaces with evolution strategies. *Comput. Struct.* **2004**, *82*, 1695–1705. [CrossRef]

32. Birkert, A.; Zimmermann, P.; Hartmann, B.; Scholle, M.; Straub, M. New Physical Scaling Approach to compensate the part contraction in drawing operations. *IOP Conf. Ser. Mater. Sci. Eng.* **2020**, *967*, 012041. [CrossRef]
33. Ouyang, D.; Feng, H.-Y. On the normal vector estimation for point cloud data from smooth surfaces. *Comput. Des.* **2005**, *37*, 1071–1079. [CrossRef]
34. Chen, S.-G.; Wu, J.-Y. Estimating normal vectors and curvatures by centroid weights. *Comput. Aided Geom. Des.* **2004**, *21*, 447–458. [CrossRef]
35. Cafuta, G.; Mole, N.; Štok, B. An enhanced displacement adjustment method: Springback and thinning compensation. *Mater. Des.* **2012**, *40*, 476–487. [CrossRef]
36. Mole, N.; Cafuta, G.; Štok, B. A 3D forming tool optimisation method considering springback and thinning compensation. *J. Mater. Process. Technol.* **2014**, *214*, 1673–1685. [CrossRef]
37. Bici, M.; Campana, F.; Cimolin, F.; Rizzo, L. Robust Die Compensation in Sheet Metal Design through the Integration of Dual Response Surface and Shape Function Optimization. Available online: https://www.hindawi.com/journals/mpe/2019/7357135/ (accessed on 22 February 2021).
38. Pegada, V.; Chun, Y.; Santhanam, S. An algorithm for determining the optimal blank shape for the deep drawing of aluminum cups. *J. Mater. Process. Technol.* **2002**, *125–126*, 743–750. [CrossRef]
39. Parsa, M.H.; Pournia, P. Optimization of initial blank shape predicted based on inverse finite element method. *Finite Elem. Anal. Des.* **2007**, *43*, 218–233. [CrossRef]
40. Azaouzi, M.; Belouettar, S.; Rauchs, G. A numerical method for the optimal blank shape design. *Mater. Des.* **2011**, *32*, 756–765. [CrossRef]
41. Naceur, H.; Guo, Y.; Batoz, J. Blank optimization in sheet metal forming using an evolutionary algorithm. *J. Mater. Process. Technol.* **2004**, *151*, 183–191. [CrossRef]
42. Park, S.H.; Yoon, J.W.; Yang, D.Y.; Kim, Y.H. Optimum blank design in sheet metal forming by the deformation path iteration method. *Int. J. Mech. Sci.* **1999**, *41*, 1217–1232. [CrossRef]
43. Chung, K.; Richmond, O. Ideal forming—I. Homogeneous deformation with minimum plastic work. *Int. J. Mech. Sci.* **1992**, *34*, 575–591. [CrossRef]
44. Yeh, F.-H.; Wu, M.-T.; Li, C.-L. Accurate optimization of blank design in stretch flange based on a forward–inverse prediction scheme. *Int. J. Mach. Tools Manuf.* **2007**, *47*, 1854–1863. [CrossRef]
45. Lin, C.-T.; Kwan, C.-T. Application of abductive network and FEM to predict the optimal blank contour of an elliptic cylindrical cup from deep drawing. *J. Mater. Process. Technol.* **2009**, *209*, 1351–1361. [CrossRef]
46. Son, K.; Shim, H. Optimal blank shape design using the initial velocity of boundary nodes. *J. Mater. Process. Technol.* **2003**, *134*, 92–98. [CrossRef]
47. Hammami, W.; Padmanabhan, R.; Oliveira, M.C.; BelHadjSalah, H.; Alves, J.L.; Menezes, L.F. A deformation based blank design method for formed parts. *Int. J. Mech. Mater. Des.* **2009**, *5*, 303–314. [CrossRef]
48. Fazli, A.; Arezoo, B. A comparison of numerical iteration based algorithms in blank optimization. *Finite Elem. Anal. Des.* **2012**, *50*, 207–216. [CrossRef]
49. Sattari, H.; Sedaghati, R.; Ganesan, R. Analysis and design optimization of deep drawing process. *J. Mater. Process. Technol.* **2007**, *184*, 84–92. [CrossRef]
50. Padmanabhan, R.; Oliveira, M.C.; Baptista, A.J.; Alves, J.L.; Menezes, L.F. Blank design for deep drawn parts using parametric NURBS surfaces. *J. Mater. Process. Technol.* **2009**, *209*, 2402–2411. [CrossRef]
51. Shim, H.; Son, K.; Kim, K. Optimum blank shape design by sensitivity analysis. *J. Mater. Process. Technol.* **2000**, *104*, 191–199. [CrossRef]
52. Mole, N.; Cafuta, G.; Štok, B. A Method for Optimal Blank Shape Determination in Sheet Metal Forming Based on Numerical Simulations. *Stroj. Vestn. J. Mech. Eng.* **2013**, *59*, 237–250. [CrossRef]
53. Rassineux, A.; Villon, P.; Savignat, J.-M.; Stab, O. Surface Remeshing by Local Hermite Diffuse Interpolation. *Int. J. Numer. Methods Eng.* **2000**, *49*, 31–49. [CrossRef]
54. Hol, J.; Meinders, V.; De Rooij, M.; Boogaard, A.V.D.; Boogaard, T.V.D. Multi-scale friction modeling for sheet metal forming: The boundary lubrication regime. *Tribol. Int.* **2015**, *81*, 112–128. [CrossRef]
55. Gil, I.; Mendiguren, J.; Galdos, L.; Mugarra, E.; De Argandoña, E.S. Influence of the pressure dependent coefficient of friction on deep drawing springback predictions. *Tribol. Int.* **2016**, *103*, 266–273. [CrossRef]